# Argon equation of state data to 1 TPa: Shock compression experiments and simulations

Seth Root,[*] Chad A. McCoy, Kyle R. Cochrane, John H. Carpenter, Raymond W. Lemke,
Luke Shulenburger, and Thomas R. Mattsson
*Sandia National Laboratories, Albuquerque, New Mexico 87185, USA*

Philip A. Sterne ●
*Lawrence Livermore National Laboratory, Livermore, California 94550, USA*

Argon is the most abundant noble gas on Earth and its noble, atomic fluid nature makes it an excellent candidate for comparison of experiment and theory at extreme conditions. We performed a combined computational and experimental study on shock compressed cryogenic liquid argon. Using Sandia's Z machine, we shock compressed liquid argon to 600 GPa and reshock states up to 950 GPa. Laser shock experiments at the Omega Laser facility extend the principal Hugoniot to 1000 GPa and provided temperature data along the principal Hugoniot. The plate impact experiments and laser shock experiments used well-characterized impedance matching standards and demonstrate consistent results between the two platforms over a common range. Density functional theory based molecular dynamics simulations provided additional data on the Hugoniot to 600 GPa. The combined experimental data and simulation results provide constraints on the development of new equation of state models at extreme conditions.

## I. INTRODUCTION

Argon is a monatomic fluid with a filled-shell configuration that makes it an ideal candidate for comparisons of experiments and theory at extreme conditions. It is the most abundant noble gas on Earth and is also found in the atmosphere of gas giant planets [1–3]. However, limited experimental data exists at extreme conditions where the electronic contribution to the equation of state (EOS) becomes important. Our earlier work on xenon [4] and krypton [5] showed that the high pressure, high temperature behavior of an EOS model can vary significantly depending on the theory used to model the electronic contribution. Lack of data leads to uncertainties in the EOS models describing argon's behavior in this regime.

Prior shock compression experiments examined initially gas or liquid argon to pressures below 200 GPa. Dattelbaum *et al.* [6] shocked compressed argon gas with initial densities ranging from 0.02 to 0.06 g/cm$^3$ to a few GPa. Chen *et al.* [7] precompressed argon gas to higher initial densities ($\sim$0.36 g/cm$^3$) and multiply shocked compressed argon up to pressures of 160 GPa. For liquid argon, planar impact experiments using explosively driven flyers [8,9] and gas-gun plate impact techniques [10] measured the Hugoniot up to 91 GPa. Gryaznov *et al.* used a convergent geometry method to measure shock states in liquid argon up to 233 GPa [11]. Additionally, Grigorev *et al.* and Voskoboinikov *et al.* made temperature measurements along the Hugoniot up to a pressure of 67 GPa and temperature of 17 000 K [9,12]. However, to constrain the EOS models in the multi-Mbar regime, we need further data at higher pressures and temperatures.

This paper presents a comprehensive experimental and computational study of cryogenic liquid argon shock compressed to 1000 GPa. We conducted magnetically accelerated flyer plate experiments on Sandia's Z machine to determine the principal Hugoniot to 600 GPa and reshock states to 950 GPa. Laser-driven, decaying shock experiments at the Omega facility provided further data on the principal Hugoniot to 1 TPa and in two experiments, provided temperature data along the principal Hugoniot. The Z and Omega data exhibited excellent consistency between the two platforms, validating both shock compression methods over the common range. We conducted density functional theory based quantum molecular dynamics simulations along the Hugoniot that provide further insight into the shock response of argon. Lastly, we compared the data to previous EOS models and report on the construction of two new global-range empirical EOS models that provide better fits to the data. Even though they were constructed based on the same data, these models deviate from each other, particularly at higher pressures. The differences between the data and the previous EOS models, and the remaining differences between the two newer models that were both fit to the data, clearly show the importance of having data at extreme conditions to constrain model EOS behavior.

## II. EXPERIMENTAL APPROACH

We conducted a series of shock and reshock compression experiments to measure the Hugoniot state and reshock state using Sandia National Laboratories' Z machine [13,14]. The Z machine is a pulsed power source capable of delivering $\sim$26 MA of current over a few 100 ns to a target. The large current produces a strong magnetic field, and the combined current and magnetic field generate a Lorentz force

_____
[*]sroot@sandia.gov
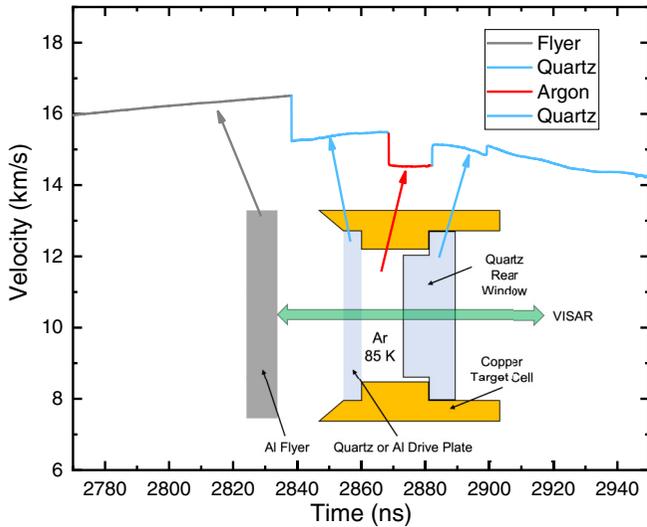
FIG. 1. Schematic view of the Z cryogenic target and a VISAR trace from a typical experiment showing the transitions from flyer to quartz drive plate to argon to rear quartz window.

$(\vec{F} = \vec{J} \times \vec{B})$ that accelerates an aluminum 6061-T6 flyer plate. The current pulse is carefully tailored to shocklessly accelerate the flyer plate to very high impact velocities and also maintain several hundred microns of solid density aluminum on the impact side of the flyer plate to produce a shock in the target [15–17]. The magnetically accelerated flyer technique has been successively refined and validated against conventional shock compression techniques [18–20].

Figure 1 shows a schematic view of the experimental configuration. The argon target configuration is similar to targets successfully fielded on the Z machine for shock compression experiments on the cryogenic liquids xenon [4] and krypton [5]. The target consisted of a copper cell body with a z-cut $\alpha$-quartz or aluminum drive plate and a z-cut, $\alpha$-quartz top-hat rear window. High purity argon gas (Matheson Trigas Research Purity >99.999%) fills the gap between the quartz windows (approximately 300 $\mu$m) to a pressure of 16.9 psi. A minicryostat [21] using liquid helium cooled the target cells to 85 K and resistive heaters attached to the target controlled the temperature to within 0.2 K. Upon reaching 85 K the argon gas condensed into liquid and the pressure in the cell dropped to 14.5 psi. Visual observation of the target cells with identical fill volumes in offline testing showed the liquid cells were completely filled and the change in target pressure was a reproducible indication the targets were completely filled with liquid argon. The initial liquid density of argon was 1.407 g/cm$^3$ using the data from Ref. [22] with an uncertainty of 0.5%. The cell windows had antireflection coatings to index match the vacuum and argon interfaces.

A velocity interferometry system for any reflector (VISAR) [23] measured the Al flyer velocities and shock velocities in the quartz drive plate, the argon sample, and the rear quartz window to within uncertainties of <0.5%. We recorded multiple VISAR signals, each with a different velocity per fringe (VPF) to eliminate $2\pi$ phase shift ambiguities in determining the shock velocities. We used an index of refraction for quartz ($n = 1.547$) and for liquid argon

($n = 1.232$) [24] to correct the VPF in each material [20]. Additionally, integrating the shock velocity with respect to time verified that the distance was consistent with the known cell dimensions.

Figure 1 shows a typical VISAR trace from a Z experiment. With the transparent quartz windows, the 532 nm laser for the VISAR passes through the target cell and reflects off the Al flyer. The VISAR tracks the Al flyer velocity up to impact on the quartz drive plate. After impact, the shock traveling in the drive plate causes the quartz to melt into a conducting fluid [20] and the VISAR directly measures the shock velocity ($U_S$) as the shock transits the quartz. The shock front in the liquid argon is also reflective providing a direct, accurate measurement of the shock velocity. As the shock transits from the argon to the rear quartz window, a reflective shock front forms in the quartz window, from which we can determine the reshock state in quartz. In two experiments we used an Al drive plate as the impedance matching standard. In this case we measured the flyer velocity just below the sample in a fused silica witness window and then used that velocity as the impact velocity on the Al drive plate. The Al drive plate is in contact with the target cell at 85 K, so we determined its density to be 2.734 g/cm$^3$ using SESAME 3700 and assumed an uncertainty of 0.5%. We also used the shock velocity measured in the fused silica witness window to account for flyer acceleration in the Al drive plate. Because we do not measure the flyer plate velocity directly in the experiments with an Al drive plate, these data have a larger uncertainty.

Additionally, we conducted three decaying shock experiments using the Omega laser facility [25] located at the University of Rochester's Laboratory for Laser Energetics. In all three experiments we determined the principal Hugoniot state to compare with the Z experiments. In two experiments we measured the temperature along the Hugoniot during the decaying shock. The Omega laser is a 60 beam frequency-tripled Nd:glass laser operating at 351 nm. The beam profiles are smoothed using eighth-order super-Gaussian phase plates with an 800 $\mu$m diameter flat top [26] and further modulated using smoothing by spectral dispersion [27]. For these experiments we used 6 to 12 beams with total laser intensity ranging from 3.9 to 8.8 $\times 10^{13}$ W/cm$^2$ and a 3 ns pulse width to generate planar shocks into the argon.

Figure 2 shows a schematic view of the experimental configuration for the Omega experiments. The target consisted of a copper cell sealed with a 60 $\mu$m thick, Z-cut $\alpha$-quartz front drive window and 100 $\mu$m thick Z-cut $\alpha$-quartz rear window. A 2 $\mu$m gold layer deposited on the front of the quartz drive window mitigated x rays and hot electrons from the laser plasma. The ablator material was a 50 $\mu$m layer of polyimide (Dupont Kapton$^{TM}$). Previous studies have shown that for polyimide ablators, a thin (2–3 $\mu$m) gold layer followed by a 60 $\mu$m thick quartz window sufficiently mitigates preheat due to hot electron generation for the laser intensities used in these experiments [28–31]. Target cells used argon gas (Airgas, Research grade, >99.9997%) cooled to 85 K—as in the Z experiments—creating a liquid argon target with initial density of 1.407 g/cm$^3$. Optical imaging using the alignment telescope for the active shock breakout (ASBO) diagnostic confirmed the argon gas condensed into liquid.

TABLE I. QMD simulation results for the liquid argon Hugoniot using the LDA functional.

| Density (g/cm$^3$) | Temperature (K) | Pressure (GPa) | $U_P$ (km/s) | $U_S$ (km/s) |
|---|---|---|---|---|
| 2.0 | 326 | 0.93 | 0.47 | 1.56 |
| 2.3 | 1197 | 4.47 | 1.13 | 2.89 |
| 2.5 | 2597 | 9.14 | 1.70 | 3.87 |
| 2.8 | 7802 | 23.6 | 2.94 | 5.77 |
| 3.2 | 13691 | 42.4 | 4.13 | 7.34 |
| 3.5 | 17677 | 59.4 | 5.05 | 8.41 |
| 4.0 | 24514 | 93.3 | 6.58 | 10.13 |
| 4.2 | 27020 | 107.6 | 7.16 | 10.74 |
| 4.5 | 31772 | 134.4 | 8.14 | 11.81 |
| 4.7 | 35580 | 156.9 | 8.87 | 12.64 |
| 5.0 | 42057 | 193.3 | 9.97 | 13.85 |
| 5.6 | 62611 | 318.9 | 13.07 | 17.43 |
| 5.8 | 74252 | 393.5 | 14.60 | 19.25 |
| 6.0 | 90616 | 503.9 | 16.61 | 21.67 |
| 6.2 | 113050 | 662.2 | 19.14 | 24.72 |

through the target. The VISAR used dual VPFs with values of 6.906 and 2.732 km/s per fringe and we adjusted the VPFs using the index of refraction values for quartz and argon as in the Z experiments to determine the in-material VPFs. Figure 2 shows a typical readout from the line VISAR streak camera where $t = 0$ corresponds to shock breakout in the quartz and shock transit into the liquid argon at approximately 3.6 ns. We analyzed the data using the Fourier transform method [33] and the uncertainty is approximately 3% of a fringe.

A streaked optical pyrometer (SOP) [34], which is sensitive to light in the 590–850 nm range, recorded the self-emission of the shock front in the quartz and the argon. Figure 2 shows the SOP recorded emission data. By correlating the SOP and VISAR records using the absolute-timing information, we can express the emission as a function of the shock velocity. We assume a gray-body approximation to convert the emission to temperature. As quartz has been extensively studied and its shock front reflectivity as a function of pressure and velocity is well known, the shock reflectivity of the argon is normalized to that of the quartz drive plate [35,36]. The gray-body

FIG. 2. Top: Schematic view of the Omega laser targets. Middle: Line VISAR raw data recorded on the streak camera At $t = 0$ ns, the shock starts in the front quartz window and transitions to the liquid argon at approximately 3.6 ns. Bottom: The SOP recorded emission data time correlated to the line VISAR data.

A line-imaging VISAR [32] measured the shock velocity in the quartz front window and the shock in the liquid argon. At the conditions reached in these experiments, the shock fronts in both the quartz and the argon were reflective allowing for a direct measurement of the shock velocity as it propagated

TABLE II. QMD simulation results for the liquid argon Hugoniot using the AM05 functional.

| Density (g/cm$^3$) | Temperature (K) | Pressure (GPa) | $U_P$ (km/s) | $U_S$ (km/s) |
|---|---|---|---|---|
| 2.0 | 346 | 2.95 | 0.71 | 2.37 |
| 2.85[a] | 7597 | 26.5 | 3.07 | 6.03 |
| 2.85[b] | 7988 | 26.8 | 3.08 | 6.06 |
| 3.8 | 21392 | 82.1 | 6.06 | 9.60 |
| 3.9 | 22743 | 89.2 | 6.37 | 9.93 |
| 4.0 | 23315 | 93.2 | 6.56 | 10.09 |
| 5.0 | 41057 | 193.7 | 9.97 | 13.84 |
| 5.6 | 61655 | 318.9 | 13.06 | 17.41 |
| 6.0 | 88779 | 495.5 | 16.46 | 21.47 |

[a]108 atoms.

[b]32 atoms.

TABLE III. The universal liquid fit parameters for the quartz Hugoniot [52]. The functional form is $U_S = a + bU_P - cU_P \exp(-dU_P)$.

| Material | $a$ | $b$ | $c$ | $d$ |
|---|---|---|---|---|
| Quartz | 5.477 | 1.242 | 2.453 | 0.4336 |

approximation gives

$$T = \frac{T_0}{\ln \frac{(1-R)A}{I}}, \tag{1}$$

where $T$, $R$, and $I$ are the temperature, reflectivity, and emission of the shock front, respectively. $T_0$ and $A$ are the calibration parameters for the Omega SOP. At the time of these experiments, the collection optics for the ASBO telescope had been recently upgraded and absolute calibration of the SOP with the new optics had not yet been carried out. An absolute calibration had recently been completed; however, the calibration coefficients were previously found to vary over time. Therefore, we judged using a relative quartz calibration was better for these experiments [34].

Because the shock velocity was approximately constant through the quartz drive plate for these shots, the shot data was insufficient to adequately constrain the fit parameters. Instead, we performed a relative calibration by extracting the quartz shock velocity and self-emission from all shots that occurred on the shot day [37]. Included with the argon experiments on that shot day were shock temperature measurements of $TiO_2$ that had decaying shocks in thick quartz samples [38]. The quartz temperature as a function of shock velocity was taken from Ref. [36] and the calculated temperature was fit to the measured emission using Eq. (1). Fit parameters calculated in this way were $T_0 = 1.88$ eV and $A = 179, 826$. Accounting for the neutral density filter (ND = 0.4) and sweep speed ($\eta = 17$ ns) used in these experiments, these values are consistent with those given in Ref. [34]. The temperature uncertainty for the argon samples calculated using these fit parameters is estimated to be 10%–15%.

## III. THEORETICAL METHODS AND RESULTS

Density functional theory (DFT) [39,40] methods are a valuable tool to elucidate the behavior of materials at extreme conditions [41,42] and the calibration of computational methods is critical for establishing the boundaries of predictive capabilities. We performed DFT, quantum molecular dynamics simulations (QMD) to calculate the principal Hugoniot of cryogenic liquid argon using the Vienna *ab initio* simulation package (VASP, ver 5.1.40) code [43,44] with the projector augmented wave (PAW) core potentials and stringent convergence settings [45]. We employed the standard psuedopotential available in the VASP package: PAW

TABLE V. The linear fit parameters and covariance matrix for the aluminum Hugoniot and for the liquid argon Hugoniot data with $U_P > 5$ km/s. The functional form is $U_S = C_0 + S_1 U_P$.

| Material | $C_0$ (km/s) | $S_1$ | $\sigma_{C_0}^2$ ($\times 10^{-3}$) | $\sigma_{S_1}^2$ ($\times 10^{-3}$) | $\sigma_{C_0}\sigma_{S_1}$ ($\times 10^{-3}$) |
|---|---|---|---|---|---|
| Aluminum | 6.322 | 1.189 | 53.58 | 0.4196 | −4.605 |
| Argon | 2.688 | 1.141 | 3.560 | 0.0177 | −0.0234 |

Ar8Apr2002 with a plane wave energy cutoff of 900 eV and complex $k$-point sampling with a mean-value point of $\frac{1}{4}, \frac{1}{4}, \frac{1}{4}$. Mermin's finite temperature formulation enforced the electron level occupations [46], which is important for QMD applied to extreme conditions [47,48].

QMD simulations depend on the choice of the approximate exchange-correlation functional. For comparison, we ran simulations using the local density approximation (LDA) [49] and the Armiento-Mattsson (AM05) [50] functionals. The AM05 exchange-correlation functional includes the generalized gradient in addition to the density and captures the effects of inhomogeneity by matching results for an Airy gas. AM05 has demonstrated high fidelity for other shock compressed noble cryogenic liquids [4,5].

The QMD simulations started from a reference state of $\rho_0 = 1.40$ g/cm³ at 85 K; similar to the experimental initial conditions. The Hugoniot energy equation is $2(E - E_{ref}) = (P + P_{ref})(V_{ref} - V)$ with $E$ the internal energy, $P$ the system pressure, $V$ the specific volume. $E_{ref}$ and $P_{ref}$ are the energy and pressure of the reference state. The reference simulation had 108 atoms and ran for 8 ps to ensure the standard deviation of the mean pressure and energy was under 1%. At low densities and temperatures, the simulations were run for multiple picoseconds at a 1.0 fs time step. At higher densities and temperatures, the time step was reduced to 0.5 fs.

The principal Hugoniot calculations used NVT molecular dynamics (fixed number of atoms, volume, and temperature) where simulations run at a specified temperature and density. The simulations used 54 atoms, but were spot checked with simulations using 108 atoms. We interpolate the Hugoniot state by running multiple simulations at a specified density with varying temperature and checking against the Hugoniot energy equation. At high compressions, the density is varied at a fixed temperature and the Hugoniot state is interpolated in density. Tables I and II list the QMD calculated Hugoniot values using the LDA functional and the AM05 functional, respectively.

## IV. RESULTS AND DISCUSSION

In the Z and Omega experiments we measured the shock velocities ($U_S$) in the quartz drive plate and the argon sample. The initial densities of the quartz drive plate and liquid

TABLE IV. The covariance matrix values to the quartz universal liquid fit used in the impedance matching analysis.

| Material | $\sigma_a^2$ ($\times 10^{-3}$) | $\sigma_a\sigma_b$ ($\times 10^{-4}$) | $\sigma_a\sigma_c$ ($\times 10^{-3}$) | $\sigma_a\sigma_d$ ($\times 10^{-4}$) | $\sigma_b^2$ ($\times 10^{-6}$) | $\sigma_b\sigma_c$ ($\times 10^{-4}$) | $\sigma_b\sigma_d$ ($\times 10^{-5}$) | $\sigma_c^2$ ($\times 10^{-2}$) | $\sigma_c\sigma_d$ ($\times 10^{-3}$) | $\sigma_d^2$ ($\times 10^{-4}$) |
|---|---|---|---|---|---|---|---|---|---|---|
| Quartz | 3.028 | −1.490 | −3.715 | −6.275 | 7.839 | 1.448 | 2.752 | 1.729 | 1.605 | 1.907 |

TABLE VI. Liquid argon principal Hugoniot data from Z (Z) and Omega (O) determined from impedance matching to quartz. The argon initial density was $1.407 \pm 0.5\%$.

| Shot | Drive plate $U_S$ (km/s) | $U_P$ (km/s) | $U_S$ (km/s) | $\rho$ (g/cm$^3$) | Pressure (GPa) |
|---|---|---|---|---|---|
| Z2601 N | $14.43 \pm 0.05$ | $9.44 \pm 0.06$ | $13.53 \pm 0.06$ | $4.655 \pm 0.086$ | $179.7 \pm 1.4$ |
| Z2601 S | $15.44 \pm 0.07$ | $10.32 \pm 0.08$ | $14.50 \pm 0.07$ | $4.878 \pm 0.115$ | $210.5 \pm 1.9$ |
| Z2232 S | $17.78 \pm 0.08$ | $12.42 \pm 0.09$ | $16.82 \pm 0.06$ | $5.373 \pm 0.131$ | $293.8 \pm 2.5$ |
| Z2528 N | $19.96 \pm 0.08$ | $14.41 \pm 0.10$ | $19.06 \pm 0.09$ | $5.772 \pm 0.159$ | $386.5 \pm 3.2$ |
| Z2528 S | $21.25 \pm 0.09$ | $15.60 \pm 0.11$ | $20.44 \pm 0.09$ | $5.940 \pm 0.169$ | $448.6 \pm 3.8$ |
| Z2229 N | $22.16 \pm 0.07$ | $16.43 \pm 0.09$ | $21.44 \pm 0.06$ | $6.025 \pm 0.127$ | $495.7 \pm 3.4$ |
| Z2233 N | $23.65 \pm 0.05$ | $17.82 \pm 0.08$ | $22.99 \pm 0.05$ | $6.262 \pm 0.105$ | $578.0 \pm 3.2$ |
| Z2233 S | $24.29 \pm 0.05$ | $18.41 \pm 0.08$ | $23.71 \pm 0.04$ | $6.297 \pm 0.098$ | $614.2 \pm 3.4$ |
| O93681 | $18.69 \pm 0.05$ | $13.26 \pm 0.06$ | $17.67 \pm 0.07$ | $5.638 \pm 0.115$ | $329.7 \pm 2.2$ |
| O93679 | $24.70 \pm 0.05$ | $18.80 \pm 0.08$ | $24.15 \pm 0.07$ | $6.345 \pm 0.120$ | $638.6 \pm 3.7$ |
| O93683 | $29.96 \pm 0.05$ | $23.72 \pm 0.10$ | $29.79 \pm 0.07$ | $6.907 \pm 0.130$ | $994.2 \pm 5.6$ |

argon were 2.65 g/cm$^3$ $\pm$ 0.3% and 1.407 g/cm$^3$ $\pm$ 0.5%. The quartz shock velocity and the weighted fit to the quartz Hugoniot data using the universal liquid Hugoniot functional form [20,51,52] give the Hugoniot state in the quartz drive plate. The fit parameters and covariance matrix are listed in Tables III and IV. To calculate the liquid argon principal Hugoniot we used a Monte Carlo impedance matching method [53], the Mie-Gruneisen, linear release (MGLR) model determined from deep release data on quartz [51,52], and the updated effective Gruneisen $\Gamma$ parameters listed in the Supplemental Material in Ref. [54].

For the two experiments (Z2229S and Z2232N) that used the Al drive plate, we determined the flyer velocity at impact using a witness window directly below the target. Using the Al Hugoniot listed in Table V and MGLR model [54,55] we do impedance matching to calculate the Hugoniot state in the argon. In shot Z2229S we observed acceleration in the fused silica (FS) witness window like that observed in Fig. 1 in the quartz drive plate. To account for acceleration in the Al drive plate, we determined the acceleration in the fused silica witness window at a distance corresponding to the thickness of the Al drive plate and applied that acceleration to the Al shock velocity at the Al/Ar interface. The acceleration in the fused silica witness window was 1% and thus the shock velocity in the Al drive plate prior to the shock transiting into the argon was assumed to be 1% higher than what the shock velocity in the aluminum was at impact with the flyer plate. Additionally in Z2229S the flyer plate shocked up, which caused a jump-off velocity of 3.62 km/s. The shock in the flyer plate caused the initial density to decrease [18] to 2.65 g/cm$^3$. We did not observe acceleration or a flyer plate shock in Z2232N. We reiterate that experiments using the aluminum drive plate have

additional uncertainty and scatter because we cannot directly measure the impact velocity of the flyer. Tables VI and VII list the liquid argon Hugoniot data determined from impedance matching to quartz and Al, respectively.

Figure 3 plots the liquid argon data in $U_S$-$U_P$ space from this work along with data from Refs. [8–11]. The experimental data from this work range from $9.5 < U_P < 24$ km/s. Over this range we observe agreement between the Z data, the laser shock data, and our QMD simulations regardless of the functional used. The liquid argon Hugoniot shows a linear trend above $U_P = 5$ km/s and for this region we calculated a weighted linear fit to the experimental data from Z, Omega, Ref. [10], and the lower pressure datum from Ref. [11]. Table V lists the fit parameters. At lower pressures ($U_P < 5$ km/s), the data diverges from our linear fit. The $U_S$-$U_P$ data exhibit curvature below $U_P < 4$ km/s that the QMD simulations are able to match. The QMD simulations suggest that the curvature in the $U_S$-$U_P$ data is very likely caused by argon transitioning from an insulator to conductor. At $U_P \sim 3.0$ km/s ($\rho = 2.85$ g/cm$^3$) argon is still an insulator with no electrons in the conduction band. Above $U_P \sim 3$ km/s, the probability of finding an electron in the conduction band increases and the band gap continuously decreases. At $U_P > 8$ km/s the band gap closes and argon is strongly conductive.

Figure 4 plots the Hugoniot data in pressure-density space where the experimental data from this work span the range from 180 to 1000 GPa. Again we observe good agreement between the Z and the Omega laser shock data through the common range up to 650 GPa. The two Z data points using the Al drive plate show consistency with the data using the quartz drive plates, although with some scatter. This agreement

TABLE VII. Liquid argon principal Hugoniot data from Z determined from impedance matching to Al. The argon initial density was $1.407 \pm 0.5\%$ and the Al drive plate (Fig. 1) initial density was 2.734 g/cm$^3$ $\pm$ 1%. Shot Z2229S had a shock in the flyer plate, which caused the reduced density.

| Shot | Flyer $\rho$ (g/cm$^3$) | Flyer $V_F$ (km/s) | Drive plate $U_P$ (km/s) | $U_P$ (km/s) | $U_S$ (km/s) | $\rho$ (g/cm$^3$) | Pressure (GPa) |
|---|---|---|---|---|---|---|---|
| Z2232N | $2.703 \pm 0.027$ | $18.21 \pm 0.16$ | $9.07 \pm 0.08$ | $11.57 \pm 0.13$ | $15.73 \pm 0.05$ | $5.320 \pm 0.169$ | $256.1 \pm 3.0$ |
| Z2229S | $2.650 \pm 0.027$ | $27.70 \pm 0.13$ | $13.92 \pm 0.11$ | $17.24 \pm 0.18$ | $22.54 \pm 0.09$ | $5.979 \pm 0.230$ | $546.6 \pm 6.3$ |
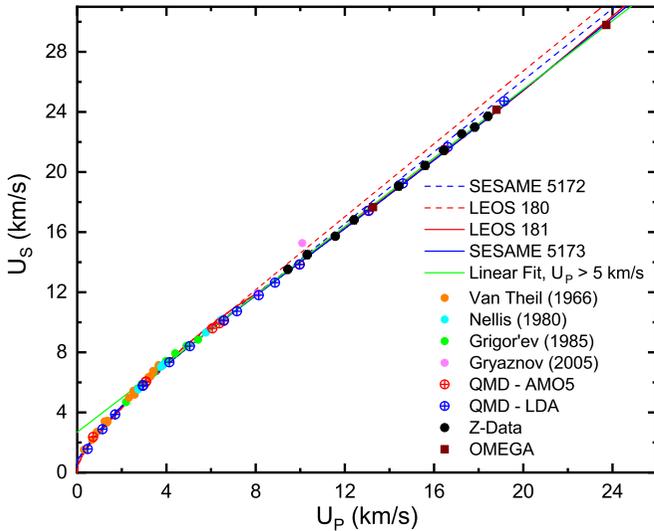
FIG. 3. The principal Hugoniot of liquid argon in $U_S$-$U_P$ space. The linear fit begins diverging from the data below $U_P \sim 4$ km/s.

emphasizes the importance of having a reliable impedance matching standard such as quartz and provides confidence in data using magnetically accelerated flyers and laser shock methods. The highest Omega datum attained a pressure of 994 GPa, which is the highest pressure data on argon to date. The QMD results show good agreement with the experimental data whether we used the AM05 or LDA functional. However, the highest pressure QMD datum at 662 GPa shows a stiffer response compared to the experimental data, but still within experimental uncertainty. At this pressure and temperature (662 GPa and 113 000 K), our VASP PAW core psuedopotential (Ar8Apr2002) is likely beginning to fail because of ionization of electrons from the core. This suggests that a new psuedopotential for argon is required for simulations at these pressures and temperatures.
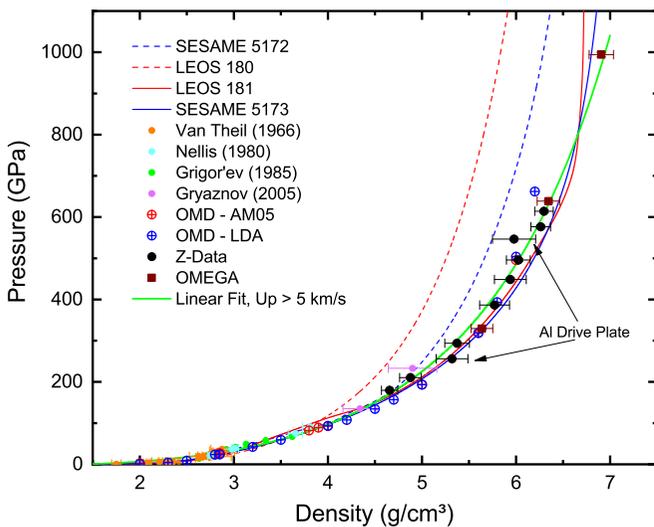


FIG. 4. The $\rho$-$P$ Hugoniot data over the full range comparing the previously published planar and converging shock data to the DFT calculations and the Z experimental results. The four tabular EOS models are also shown for comparison.

Prior to this work, two argon EOS models were available: LEOS 180 developed using the QEOS [56] methodology, and SESAME 5172 [57] that was based upon a complicated set of models. Figures 3 and 4 show the EOS models in comparison to the experimental data. Both LEOS 180 and SESAME 5172 are significantly stiffer (less compressible) than the experimental data and diverge from each other around 90 GPa. However, we note these models had access to limited experimental data up to 90 GPa, and exemplifies the difficulty in extrapolating models to regions where there is no constraining data. Given the stiffness of both models in comparison to the high pressure shock experiments, two new argon EOS models were developed: SESAME 5173 and LEOS 181.

The SESAME 5173 model was developed with the aim of improving agreement not only with the high pressure Hugoniot, but also lower temperature data for fluid and solid argon, including its phase boundaries. It utilized techniques similar to those used for xenon [58]. In particular, the CRIS [59] model, shown to be excellent in describing the noble gases [60], comprised the ion-thermal component for the fluid, with a standard Debye model for the solid. These were calibrated to pressure-volume-temperature data, melt and vaporization data, as well as Hugoniot data with an initial solid state. The Bushman-Lomonosov-Fortov semiempirical model [61] was then added as the electron-thermal component, and calibrated to the Z Hugoniot data for the liquid, with the ion-thermal components fixed. Finally, at high temperatures, the 5173 model transitions to the Thomas-Fermi-Kirzhnits model. More details on the development of SESAME 5173 may be found in Ref. [62].

The LEOS 181 is a global-range equation of state table that was made using a QEOS approach [56,63] similar to LEOS 180. There were two significant differences from the approach used in LEOS 180. First, LEOS 181 uses an electron-thermal contributions from atom-in-jellium electronic structure calculations using the Purgatorio code [64,65] instead of the more commonly used Thomas-Fermi [66] form. This provides a realistic description of the effects of atomic shell structure on the EOS that captures both the relatively low electron-thermal pressure contribution at low temperatures in the inert-gas limit and the variations in heat capacity associated with ionization at higher pressures and temperatures. Second, LEOS 181 uses a flexible polynomial-based form for the Grueneisen $\Gamma$ as a function of density, in contrast to the piecewise linear approach used in LEOS 180. Like SESAME 5173, LEOS 181 was fit to a range of low temperature data at and near equilibrium conditions as well as diamond anvil cell (DAC) [67] and shock compression data [9,10,68], together with the Z machine data in this work. In constructing the EOS, only the cold-curve and ion-thermal components were adjusted to fit the suite of experimental data; no adjustments were made to the electron-thermal contributions. After the cold curve was adjusted to satisfy equilibrium conditions and the DAC data [67], the Hugoniot data were fit primarily by adjusting the Gruneisen $\Gamma$ term using the increased flexibility provided by the polynomial form.

The SESAME and LEOS models both show good results in matching the experimental data across a wide range of parameter space. Along the Hugoniot, the models replicate the Z and Omega data within the uncertainties, although between 400

FIG. 5. Top: Temperature along the Hugoniot determined from prior Hugoniot experiments, laser-driven decaying shocks at Omega, QMD calculations, and the tabular EOS models. Bottom: Zoomed in view the of Hugoniot temperature in $T$-$P$ space at lower pressures.

unknown systematic error in using Omega at those pressures when compared to Z data. Prior work on MgO [31] and fused silica [69] also show this softening trend at high pressures. Further comparisons of magnetically accelerated flyer plates and laser shock data at these extreme pressures are needed.

Figure 5 shows the experimentally measured Hugoniot temperatures from the prior work [9,12], our laser-driven decaying shock experiments, QMD simulations, and the four EOS models. The laser shock measurements provide temperature as a function of shock velocity and we used the argon Hugoniot linear fit in Table V to convert from $U_S$ to $P$ as the shock decays transiting the argon. Our temperature measurements and QMD simulations show good agreement between 100 and 600 GPa regardless of whether we used the AM05 or LDA functionals. Additionally, the QMD simulations show good agreement with the prior work below 75 GPa. The two new EOS models predict temperatures consistent with the QMD simulations and within the uncertainty of the laser shock experimental data. However, we observe that the LEOS 181 and SESAME 5173 tables show a difference in temperature along the Hugoniot because of the different models used in their construction.

The Z target geometry permits the measurement of a reshock state in the argon when the shock transits from the argon into the rear quartz window. The shock front in the rear quartz window is reflective and we accurately measure the shock velocity in the quartz. With this measurement and the Hugoniot fit to quartz, we know accurately the particle velocity ($U_P$) and pressure ($P$) in the argon reshock state because $P$ and $U_P$ must be equal at the interface. The reshock states are calculated using a MCIM method similar to that used for the principal Hugoniot [53]. The argon shock velocity is not constant as it traverses the sample. We use the measured argon shock velocity just prior to the shock transiting into the quartz rear window and the weighted linear fit to the argon Hugoniot data listed in Table V to determine the initial state of argon prior to the reshock. Table VIII lists the reshock data from the Z experiments.

Figure 6 shows the experimental reshock data compared to SESAME 5173 and LEOS 181. The black symbols are the experimental reshock data and the corresponding initial state determined using the argon shock velocity in Table VIII and the linear fit to the argon prinicpal Hugoniot in Table V. The blue and red lines plot the principal Hugoniot from 5173 and

and 700 GPa, both models trend to being more compressible than the data. At pressures above 700 GPa the models show a different response with the LEOS 181 model becoming slightly stiffer, which is caused by the different methods used in modeling the electron-thermal component in the EOS. Both models are slightly stiffer when compared to the highest-pressure point from Omega at ∼1000 GPa and the linear fit above 800 GPa. We note that it is possible that the Omega data at ∼1000 GPa could be more compressible because of an

TABLE VIII. Experimental reshock data for argon showing the measured shock velocities in the argon prior to shock transit into the quartz and the quartz rear window along with the final density-pressure state in the reshocked argon.

| Shot | Argon $U_S$ (km/s) | Quartz $U_S$ (km/s) | $\rho_2$ (g/cm$^3$) | Pressure (GPa) |
|---|---|---|---|---|
| Z2601 N | 13.56 ± 0.06 | 14.18 ± 0.08 | 5.747 ± 0.167 | 284.4 ± 3.8 |
| Z2601 S | 14.49 ± 0.07 | 15.13 ± 0.06 | 6.023 ± 0.166 | 330.0 ± 3.2 |
| Z2232 N | 15.74 ± 0.04 | 16.46 ± 0.04 | 6.265 ± 0.102 | 400.5 ± 2.6 |
| Z2232 S | 16.58 ± 0.08 | 17.20 ± 0.05 | 6.618 ± 0.181 | 443.2 ± 3.3 |
| Z2528 N | 18.58 ± 0.09 | 19.28 ± 0.11 | 6.893 ± 0.224 | 576.4 ± 7.8 |
| Z2528 S | 19.84 ± 0.08 | 20.44 ± 0.09 | 7.239 ± 0.205 | 659.3 ± 6.9 |
| Z2229 N | 21.04 ± 0.06 | 21.61 ± 0.06 | 7.443 ± 0.148 | 749.0 ± 5.3 |
| Z2229 S | 22.47 ± 0.10 | 22.86 ± 0.10 | 7.872 ± 0.259 | 851.6 ± 8.9 |
| Z2233 N | 22.82 ± 0.06 | 23.21 ± 0.06 | 7.905 ± 0.162 | 881.7 ± 5.9 |
| Z2233 S | 23.65 ± 0.04 | 23.97 ± 0.05 | 8.087 ± 0.134 | 948.7 ± 5.3 |
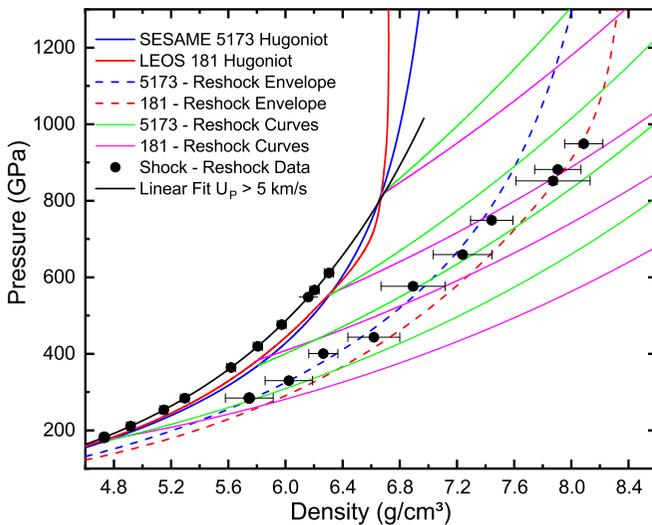
FIG. 6. Argon reshock data. The black symbols show the corresponding Z Hugoniot and reshock data. The blue and red solid lines plot the SESAME 5173 and LEOS 181 principal Hugoniots, respectively, with the green and magenta lines showing the reshock states. The blue and red dash lines are the envelope of reshock end states determined using the 5173 or 181 table and the quartz Hugoniot.

181, respectively. The green and the magenta lines are reshock Hugoniots calculated using 5173 and 181 from the same density point along the principal Hugoniot. The reshock curves (green and magenta) show that for a given pressure, LEOS 181 is more compressible. To compare to the experimental data, we calculate the loci of reshock states using the EOS models and impedance matching to the quartz Hugoniot in Table III. The blue and red dashed lines are loci of end states for a reshock from the Hugoniot. While both models do not match the reshock data exactly because their principal Hugoniots are more compressible than the fit to the experimental data, the models do trend with the data. At reshock pressures below 800 GPa, the SESAME 5173 table matches the compressibility observed in the data; however, at the highest reshock pressures the LEOS 181 table does a better job of matching the compressibility observed in the reshock data. Neither the SESAME 5173 nor LEOS 181 table used the reshock data in their model calibrations. The reshock data provide a challenging additional constraint for the EOS models and the current EOS tables show deviations on the reshock that users should note.

## V. SUMMARY AND CONCLUSIONS

We experimentally determined complete EOS data (density, pressure, and temperature) for shock compressed liquid argon up to 1000 GPa—the highest pressures attained in argon published to date. Comparisons between the Z data and the Omega data show they are in good agreement over the common range of density and pressure, which provides confidence in both platforms and demonstrates the importance of having common, well-characterized Hugoniot standards for impedance matching. The QMD simulations are able to reproduce the $P$-$\rho$ Hugoniot data and the temperature along the Hugoniot, suggesting that for argon the shock response is insensitive to the choice of functional. At 662 GPa, however, the QMD begins to deviate stiffer compared to experimental data likely because core electrons begin to play a role in the high pressure-temperature response and our psuedopotential is no longer valid. Lastly, the two new EOS models developed using the data presented here provide validated models for use up to pressures of 1 TPa and temperatures of 100 000 K. Although these models utilized the same data for calibration, they still show differences in the Hugoniot temperature, the Hugoniot at pressures above 800 GPa, and in modeling the reshock. Our results demonstrate the importance of having data at extreme conditions to calibrate EOS model behavior.

[1] S. K. Atreya, P. R. Mahaffy, H. B. Neimann, M. H. Wong, and T. C. Owen, Planet. Space Sci. **51**, 105 (2003).

[2] F. Hersant, D. Gautier, and J. I. Lunine, Planet. Space Sci. **52**, 623 (2004).

[3] O. Mousis, J. I. Lunine, J.-M. Petit, S. Picaud, B. Schmitt, D. Marquer, J. Horner, and C. Thomas, Astrophys. J. **714**, 1418 (2010).

[4] S. Root, R. J. Magyar, J. H. Carpenter, D. L. Hanson, and T. R. Mattsson, Phys. Rev. Lett. **105**, 085501 (2010).

[5] T. R. Mattsson, S. Root, A. E. Mattsson, L. Shulenburger, R. J. Magyar, and D. G. Flicker, Phys. Rev. B **90**, 184105 (2014).

[6] D. M. Dattelbaum, P. M. Goodwin, D. B. Garcia, R. L. Gustavsen, J. M. Lang, T. D. Aslam, S. A. Sheffield, L. L. Gibson, and J. S. Morris, AIP Conf. Proc. **1793**, 090004 (2017).

[7] Q. F. Chen, J. Zheng, Y. J. Gu, Y. L. Chen, L. C. Cai, and Z. J. Shen, J. Chem. Phys. **140**, 074202 (2014).

[8] M. van Thiel and B. J. Alder, J. Chem. Phys. **44**, 1056 (1966).

[9] F. V. Grigor'ev, S. B. Kormer, O. L. Mikhailova, M. A. Mochalov, and V. D. Urlin, Zh. Eksp.Teor. Fiz. **88**, 1271 (1985) [Sov. Phys. JETP **61**, 751 (1985)].

[10] W. J. Nellis and A. C. Mitchell, J. Chem. Phys. **73**, 6137 (1980).

[11] V. K. Gryaznov, M. V. Zhernokletov, I. L. Iosilevsky, S. I. Kirshanov, V. B. Mintsev, A. L. Mikhailov, A. B. Mezhevov, M. A. Mochalov, V. E. Fortov, and A. N. Shuikin, in *Proceedings of the VII Khariton Conference, in Russian*, edited by A. L. Mikhailov (Russian Federal Nuclear Center - All Russia Research Institute of Experimental Physics. 2005), p. 326.

[12] I. M. Voskoboinikov, M. F. Gogulya, and Y. A. Dolgoborodov, Dokl. Akad. Nauk SSSR **246**, 579 (1979).

[13] M. K. Matzen, Phys. Plasmas **4**, 1519 (1997).

[14] M. E. Savage, L. F. Bennett, D. E. Bliss, W. T. Clark, R. S. Coats, J. M. Elizondo, K. R. LeChien, H. C. Harjes, J. M. Lehr, J. E. Maenchen *et al.*, in *2007 16th IEEE International Pulsed Power Conference*, Vol. 2 (IEEE, Piscataway, NJ, 2007), pp. 979–984.

[15] R. W. Lemke, M. D. Knudson, C. A. Hall, T. A. Haill, M. P. Desjarlais, J. R. Asay, and T. A. Mehlhorn, Phys. Plasmas **10**, 1092 (2003).

[16] R. W. Lemke, M. D. Knudson, D. E. Bliss, K. Cochrane, J.-P. Davis, A. A. Giunta, H. C. Harjes, and S. A. Slutz, J. Appl. Phys. **98**, 073530 (2005).

[17] R. W. Lemke, M. D. Knudson, and J.-P. Davis, Int. J. Impact Engng. **38**, 480 (2011).

[18] M. D. Knudson, R. W. Lemke, D. B. Hayes, C. A. Hall, C. Deeney, and J. R. Asay, J. Appl. Phys. **94**, 4420 (2003).

[19] M. D. Knudson, D. L. Hanson, J. E. Bailey, C. A. Hall, J. R. Asay, and C. Deeney, Phys. Rev. B **69**, 144209 (2004).

[20] M. D. Knudson and M. P. Desjarlais, Phys. Rev. Lett. **103**, 225501 (2009).

[21] D. L. Hanson, A. J. Lopez, M. D. Knudson, S. Root, M. E. Cuneo, K. P. Shelton, J. M. Villalva, J. R. Asay, and D. G. Schroen, Cryogenic targets for dynamic material properties and fusion studies at Sandia National Laboratories, Tech. Rep. SAND2011-7027C (Sandia National Laboratories, USA, 2011), https://www.osti.gov/biblio/1118639.

[22] A. C. Sinnock, J. Phys. C: Solid State Phys. **13**, 2375 (1980).

[23] L. M. Barker and R. E. Hollenbach, J. Appl. Phys. **43**, 4669 (1972).

[24] A. C. Sinnock and B. L. Smith, Phys. Rev. **181**, 1297 (1969).

[25] T. Boehly, D. Brown, R. Craxton, R. Keck, J. Knauer, J. Kelly, T. Kessler, S. Kumpan, S. Loucks, S. Letzring, F. Marshall, R. McCrory, S. Morse, W. Seka, J. Soures, and C. Verdon, Opt. Commun. **133**, 495 (1997).

[26] Y. Lin, T. J. Kessler, and G. N. Lawrence, Opt. Lett. **20**, 764 (1995).

[27] S. Skupsky, R. W. Short, T. Kessler, R. S. Craxton, S. Letzring, and J. M. Soures, J. Appl. Phys. **66**, 3456 (1989).

[28] S. Brygoo, E. Henry, P. Loubeyre, J. Eggert, M. Koenig, B. Loupias, A. Benuzzi-Mounaix, and M. R. Le Gloahec, Nat. Mater. **6**, 274 (2007).

[29] M. A. Barrios, D. G. Hicks, T. R. Boehly, D. E. Fratanduono, J. H. Eggert, P. M. Celliers, G. W. Collins, and D. D. Meyerhofer, Phys. Plasmas **17**, 056307 (2010).

[30] M. Millot, N. Dubrovinskaia, A. Cernok, S. Blaha, L. Dubrovinsky, D. G. Braun, P. M. Celliers, G. W. Collins, J. H. Eggert, and R. Jeanloz, Science **347**, 418 (2015).

[31] C. A. McCoy, M. C. Marshall, D. N. Polsin, D. E. Fratanduono, P. M. Celliers, D. D. Meyerhofer, and T. R. Boehly, Phys. Rev. B **100**, 014106 (2019).

[32] P. M. Celliers, D. K. Bradley, G. W. Collins, D. G. Hicks, T. R. Boehly, and W. J. Armstrong, Rev. Sci. Instrum. **75**, 4916 (2004).

[33] P. M. Celliers, G. W. Collins, L. B. Da Silva, D. M. Gold, and R. Cauble, Appl. Phys. Lett. **73**, 1320 (1998).

[34] M. C. Gregor, R. Boni, A. Sorce, J. Kendrick, C. A. McCoy, D. N. Polsin, T. R. Boehly, P. M. Celliers, G. W. Collins, D. E. Fratanduono, J. H. Eggert, and M. Millot, Rev. Sci. Instrum. **87**, 114903 (2016).

[35] D. G. Hicks, T. R. Boehly, J. H. Eggert, J. E. Miller, P. M. Celliers, and G. W. Collins, Phys. Rev. Lett. **97**, 025502 (2006).

[36] P. M. Celliers, P. Loubeyre, J. H. Eggert, S. Brygoo, R. S. McWilliams, D. G. Hicks, T. R. Boehly, R. Jeanloz, and G. W. Collins, Phys. Rev. Lett. **104**, 184503 (2010).

[37] K. Falk, C. A. McCoy, C. L. Fryer, C. W. Greeff, A. L. Hungerford, D. S. Montgomery, D. W. Schmidt, D. G. Sheppard, J. R. Williams, T. R. Boehly, and J. F. Benage, Phys. Rev. E **90**, 033107 (2014).

[38] S. Duwal, C. A. McCoy, P. F. Weck, P. Kalita, H. L. Hanshaw, K. Cochrane, T. Ao, and S. Root, Phys. Rev. B **102**, 024105 (2020).

[39] P. Hohenberg and W. Kohn, Phys. Rev. **136**, B864 (1964).

[40] W. Kohn and L. J. Sham, Phys. Rev. **140**, A1133 (1965).

[41] M. D. Knudson, M. P. Desjarlais, and D. H. Dolan, Science **322**, 1822 (2008).

[42] S. Root, J. P. Townsend, E. Davies, R. W. Lemke, D. E. Bliss, D. E. Fratanduono, R. G. Kraus, M. Millot, D. K. Spaulding, L. Shulenburger, S. T. Stewart, and S. B. Jacobsen, Geophys. Res. Lett. **45**, 3865 (2018).

[43] G. Kresse and J. Hafner, Phys. Rev. B **47**, 558 (1993).

[44] G. Kresse and J. Furthmüller, Phys. Rev. B **54**, 11169 (1996).

[45] A. E. Mattsson, P. A. Schultz, M. P. Desjarlais, T. R. Mattsson, and K. Leung, Model. Simul. Mater. Sci. Eng. **13**, R1 (2005).

[46] N. Mermin, Phys. Rev. **137**, A1441 (1965).

[47] M. P. Desjarlais, Phys. Rev. B **68**, 064204 (2003).

[48] T. R. Mattsson and M. P. Desjarlais, Phys. Rev. Lett. **97**, 017801 (2006).

[49] J. P. Perdew and A. Zunger, Phys. Rev. B **23**, 5048 (1981).

[50] R. Armiento and A. E. Mattsson, Phys. Rev. B **72**, 085108 (2005).

[51] M. D. Knudson and M. P. Desjarlais, Phys. Rev. B **88**, 184107 (2013).

[52] M. P. Desjarlais, M. D. Knudson, and K. R. Cochrane, J. Appl. Phys. **122**, 035903 (2017).

[53] S. Root, K. R. Cochrane, J. H. Carpenter, and T. R. Mattsson, Phys. Rev. B **87**, 224102 (2013).

[54] M. D. Knudson and M. P. Desjarlais, Phys. Rev. Lett. **118**, 035501 (2017).

[55] M. D. Knudson, M. P. Desjarlais, and A. Pribram-Jones, Phys. Rev. B **91**, 224105 (2015).

[56] R. M. More, K. H. Warren, D. A. Young, and G. B. Zimmerman, Phys. Fluids **31**, 3059 (1988).

[57] J. Wolford and K. Long, *A New Theoretical EOS for Argon*, Tech. Rep. H-Division Quarterly Report UCID-18574-81-3 (Lawrence Livermore National Laboratory, 1981).

[58] J. H. Carpenter, D. G. Flicker, S. Root, R. J. Magyar, D. L. Hanson, and T. R. Mattsson, EPJ Web Conf. **10**, 00018 (2010).

[59] G. I. Kerley, J. Chem. Phys. **73**, 478 (1980).

[60] G. I. Kerley and P. M. Henry, Theoretical equations of state for the rare gases, Tech. Rep. LA-8062 (Los Alamos Scientific Laboratory, USA, 1980), https://www.osti.gov/biblio/5607235.

[61] A. V. Bushman *et al.*, *Intense Dynamic Loading of Condensed Matter* (Taylor & Francis, Washington DC, 1993).

[62] J. H. Carpenter, S. Root, K. R. Cochrane, D. G. Flicker, and T. R. Mattsson, Equation of state of Argon: Experiments on Z, Density Functional Theory (DFT) simulations, and wide-range model, Tech. Rep. SAND2012-7991 (Sandia National Laboratories, USA, 2012), https://www.osti.gov/biblio/1055655.

[63] D. A. Young and E. M. Corey, J. Appl. Phys. **78**, 3748 (1995).

[64] B. Wilson, V. Sonnad, P. Sterne, and W. Isaacs, J. Quant. Spectrosc. Radiat. Transfer **99**, 658 (2006).

[65] P. A. Sterne, S. B. Hansen, B. G. Wilson, and W. A. Isaacs, High Energy Density Phys. **3**, 278 (2007).

[66] R. P. Feynman, N. Metropolis, and E. Teller, Phys. Rev. **75**, 1561 (1949).

[67] L. W. Finger, R. M. Hazen, G. Zou, H. K. Mao, and P. M. Bell, Appl. Phys. Lett. **39**, 892 (1981).

[68] S. P. Marsh, *LASL Shock Hugoniot Data* (University of California Press, Berkeley, 1980), Vol. 5.

[69] S. Root, J. P. Townsend, and M. D. Knudson, J. Appl. Phys. **126**, 165901 (2019).